Elastic scattering and α-particle production in ^{6}He + ^{208}Pb collisions at 22 MeV

L. Acosta,[*] A. M. Sánchez-Benítez, M. E. Gómez, I. Martel, F. Pérez-Bernal, F. Pizarro, J. Rodríguez-Quintero, and K. Rusek[†]
Departamento de Física Aplicada, Universidad de Huelva, E-21071 Huelva, Spain

M. A. G. Alvarez,[‡] M. V. Andrés, J. M. Espino, J. P. Fernández-García,[‡] J. Gómez-Camacho,[‡] and A. M. Moro
Departamento de Física Atómica, Molecular y Nuclear, Universidad de Sevilla, Apdo. 1065, E-41080 Sevilla, Spain

C. Angulo,[§] J. Cabrera, E. Casarejos,[‖] and P. Demaret
Institut de Physique Nucléaire and Centre de Recherches du Cyclotron, Université Catholique de Louvain, B-1348 Louvain-la Neuve, Belgium

M. J. G. Borge, D. Escrig,[¶] and O. Tengblad
Instituto de Estructura de la Materia, CSIC, E-28006 Madrid, Spain

S. Cherubini, P. Figuera, and M. Gulino
INFN Laboratori Nazionali del Sud, I-95123 Catania, Italy

M. Freer, C. Metelko, and V. Ziman
School of Physics and Astronomy, University of Birmingham, B15 2TT Birmingham, United Kingdom

R. Raabe, I. Mukha,[**] and D. Smirnov[††]
Instituut voor Kern-en Stralingsfysica, Katholieke Universiteit Leuven, B-3001 Leuven, Belgium

O. R. Kakuee
Van de Graaff Laboratory, Nuclear Science School, NSTRI, P.O. Box 14395-836, Tehran, Iran

J. Rahighi
Institute for Research in Fundamental Sciences, IPM, School of Particles Accelerators, P.O. Box 19395-5746, Tehran, Iran

(Received 17 March 2011; published 6 October 2011)

Experimental results of the elastic scattering of ^{6}He on ^{208}Pb at $E_{\mathrm{LAB}} = 22$ MeV, measured at the CRC facility (Louvain-la-Neuve, Belgium), are presented, including results on the ^{4}He production channel. These data were taken with full angular coverage and high angular resolution. Both experimental cross sections are compared with continuum discretized coupled channels and distorted-wave Born approximation calculations, where direct breakup and transfer to the continuum processes are considered. The elastic data confirm the absence of the Coulomb rainbow, while the distribution of α particles indicates that such production is mostly generated by transfer to the continuum.

DOI: 10.1103/PhysRevC.84.044604 PACS number(s): 25.60.−t, 24.50.+g, 25.70.Mn, 25.70.Hi

I. INTRODUCTION

Nuclear systems such as ^{6}He and ^{11}Li are known to have an extended neutron distribution called halo [1]. These systems can be described as a core surrounded by two valence neutrons. The occurrence of nuclear halos are within the most interesting properties of light exotic nuclei. A special feature of these two-neutron halo nuclei is that any subsystem (core + $1n$, $1n + 1n$) is unbound, and that is the reason why these nuclei are often referred as Borromean nuclei [2].

Up to now there has been intense scientific activity, both theoretical and experimental, in order to understand the basic structure of the halo states. Much of this work has been dedicated to the study of the single-particle states of the valence neutrons by means of quasifree nucleon-knockout reactions with high-energy beams [3]. However, it is still important to study the collective aspects of the halo such as the

[*]Presently at INFN Laboratori Nazionali del Sud, I-95123 Catania, Italy; luis.acosta@dfa.uhu.es; acosta@lns.infn.it.
[†]Also at Heavy Ion Laboratory, University of Warsaw, Pasteura 5a, PL-02093 Warsaw, Poland.
[‡]Also at Centro Nacional de Aceleradores, Av. Thomas A. Edison, E-41092 Sevilla, Spain.
[§]Presently at Tractebel Engineering S.A., Avenue Ariane 7, B-1200 Brussels, Belgium.
[‖]Presently at Universidade de Vigo, E-36310 Vigo, Spain.
[¶]Presently at Consejo de Seguridad Nuclear, c/Justo Dorado, 11 E-28040 Madrid, Spain.
[**]Presently at GSI Helmholtzzentrum für Schwerionenforschung, D-64291 Darmstadt, Germany.
[††]Presently at Atys Concept, F-33210 Arcachon, France.

characteristic nuclear excitations, the coupling of these collective states to the continuum, and the role of halo-core correlations. These properties will manifest themselves especially in collisions at energies around the Coulomb barrier where Coulomb excitation, transfer, and breakup reactions play a dominant role.

The ^{6}He nucleus exhibits many remarkable features: it consists of a tightly bound core (α particle) and two loosely bound neutrons ($S_{2n} = 0.97$ MeV), and it is β unstable ($T_{1/2} = 807$ ms). The elastic scattering of ^{6}He on ^{208}Pb at different bombarding energies near the Coulomb barrier has been studied in previous works [4–6]. It has been shown that the angular distribution of the ratio of the elastic over the Rutherford cross sections departs from the characteristic Fresnel pattern expected for heavy-ion scattering at these energies. The characteristic rainbow peak present in collisions with stable heavy ions is partially or completely suppressed in the case of ^{6}He. This effect on elastic scattering arises from the weakly bound nature of the projectile, which makes the coupling to the continuum relevant and can significantly affect the dynamics of the collision.

^{6}He scattering on ^{208}Pb at 22 MeV, just above the Coulomb barrier of the system (∼19 MeV), has been studied previously in Ref. [6], but the range of angles was limited. Here we present experimental results on elastic scattering that comprise the missing angular region in the previous work and also include measurements at several common angles to test the consistency between measurements. In addition, experimental data of the α particles produced from the projectile-target interaction are also reported for the same angular range, since the detection system used in this experiment allowed the identification of ^{4}He and ^{6}He separately, by means of a set of nine telescopes distributed so that the maximum angular range could be covered.

Various theoretical calculations have been performed in order to reproduce the different experimental angular distributions and to interpret them accordingly. These are based on continuum discretized coupled channels (CDCC) and distorted-wave Born approximation (DWBA) calculations [7–10]. In the following sections we describe the experimental setup and the subsequent data analysis. Then we present our experimental results along with some calculations. In the last section we summarize the main conclusions of this work.

II. EXPERIMENT

The experiment was performed at the Cyclotron Research Centre (CRC) of the Université Catolique de Louvain-la-Neuve (Belgium) facility [11], where a high-intensity ^{6}He beam can be produced. The ^{6}He beam was generated using the proton beam at 30 MeV from the cyclotron Cyclon-30 impinging on a LiF powder target, via the reaction ^{7}Li(p,2p)^{6}He. The atomic ^{6}He is then ionized in a electron cyclotron resonance (ECR) ion source and post-accelerated in a second cyclotron, the Cyclone-110, operated in a way that suppresses almost completely the isobaric contamination [12].

The secondary ^{6}He beam was produced in the 2^{+} charge state and accelerated up to 22 MeV with a typical intensity on the scattering target of 1×10^{5} particles/s. A high-intensity

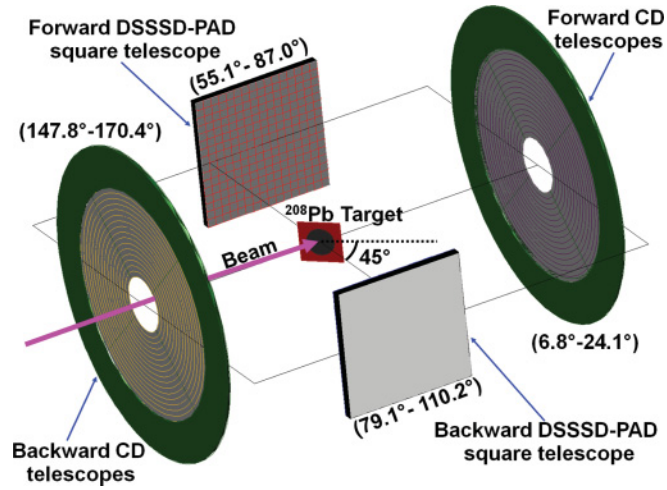

FIG. 1. (Color online) Sketch of the experimental setup. The LAB scattering angles covered by each telescope are indicated.

^{4}He beam at a laboratory energy of 12 MeV was utilized for the normalization of the elastic cross section. The target was a self-supporting foil of ^{208}Pb with a thickness of 1.12 mg/cm^{2}. It is important to mention that the beam was large and that it was reduced to less than 5 mm by a collimator upstream.

The reaction products were registered using one of the possible configurations of the DINEX silicon detector array [13–15]. The experimental setup is shown schematically in Fig. 1. This particular configuration was composed of two groups of telescopes. Each telescope is formed by a 40-μm-thick silicon strip ΔE detector, radially segmented in 16 strips, and a 500-μm-thick PAD E detector. The 90° circular sector geometry of the telescopes makes it possible to assemble four of them in a CD-like shape (i.e. with the shape of a Compact Disk). These CD telescopes were then placed inside the DINEX reaction chamber, one at forward angles (CD-forward) and the other at backward angles (CD-backward). The angular range in the laboratory reference frame (LAB) covered by the CD-forward was of 6.8°–24.1° whereas the CD-backward covered the 147.8°–170.4° angular range. A copper shield was placed over the first five innermost strips of the CD-forward telescope to protect them against the high counting rate expected at those angles. The final angular range for the CD-forward telescope, after suppressing the strips closest to the beam, was 13.0°–24.1°.

The setup also included two square telescopes located at intermediate angles, denoted as square-forward and square-backward. These telescopes consisted of a square 5×5 cm^{2}, 60-μm-thick double-sided silicon strip ΔE detector (DSSSD) with 16 strips in each side, mutually orthogonal, and a 1500-μm-thick, square PAD E detector. The spatial distribution provided by these two telescopes fulfilled a two-folded purpose: to cover a large angular range (55°–110°) while keeping an overlapping region (79°–87°) large enough to allow getting a proper match between them in the subsequent analysis. The target was tilted 45° with respect to the beam axis in order to ensure the detection of the outgoing particles in the angular range around 90°.

A triple ^{239}Pu-^{241}Am-^{244}Cm α-particle source and the elastically scattered ^{6}He and ^{4}He nuclei were used for the energy calibration of the detectors. A low-rate pulse generator (pulser) was used to send a test signal to all the preamplifiers during the experiment, to evaluate the relative efficiency of the electronic chain attached to every detector with respect to the others, as well as the global dead time of the data acquisition.

The energy and time (with respect to the cyclotron radiofrequency) signals were recorded for each event, defined as a logic "OR" of all detectors. The trigger rate from the CD-forward telescope was scaled down by a known factor during the measurements with the ^{4}He beam by means of a rate-divider module.

III. DATA ANALYSIS

A. Particle identification

Due to the particularities of the different parts of the detection system, the analysis was split as follows: (i) forward angles (CD-forward telescopes), (ii) backward angles (CD-backward telescopes), and (iii) side angles (square telescopes).

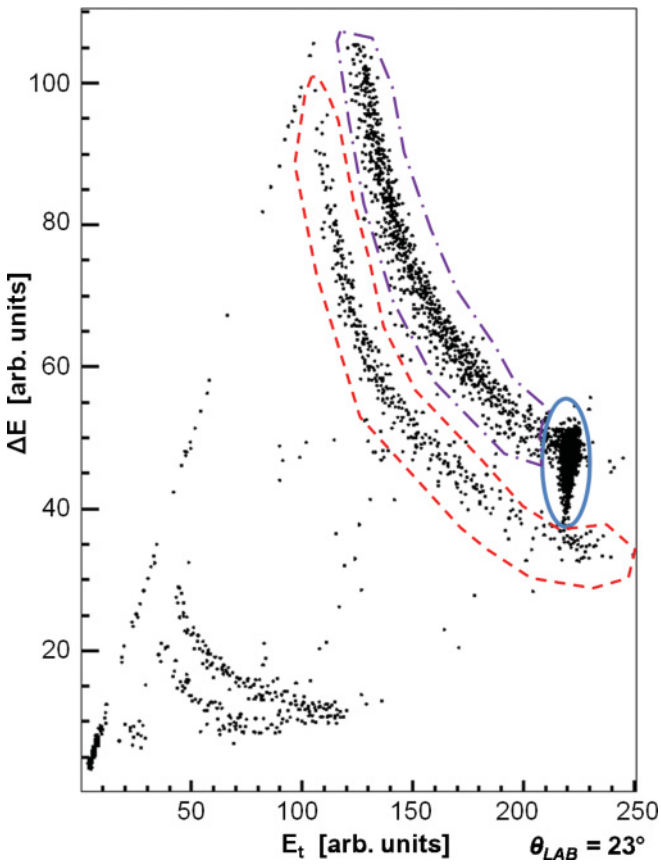

FIG. 2. (Color online) Typical particle identification spectrum ΔE-E_t of one strip from the CD-forward telescope, obtained with the ^{6}He beam at $E_{\mathrm{LAB}} = 22$ MeV. The solid line ellipsoid encloses events corresponding to elastically scattered ^{6}He. The dashed polygon encloses ^{4}He fragments. The dot-dashed polygon encloses ^{6}He scattered in some elements of the setup other than the ^{208}Pb target (see text for details).

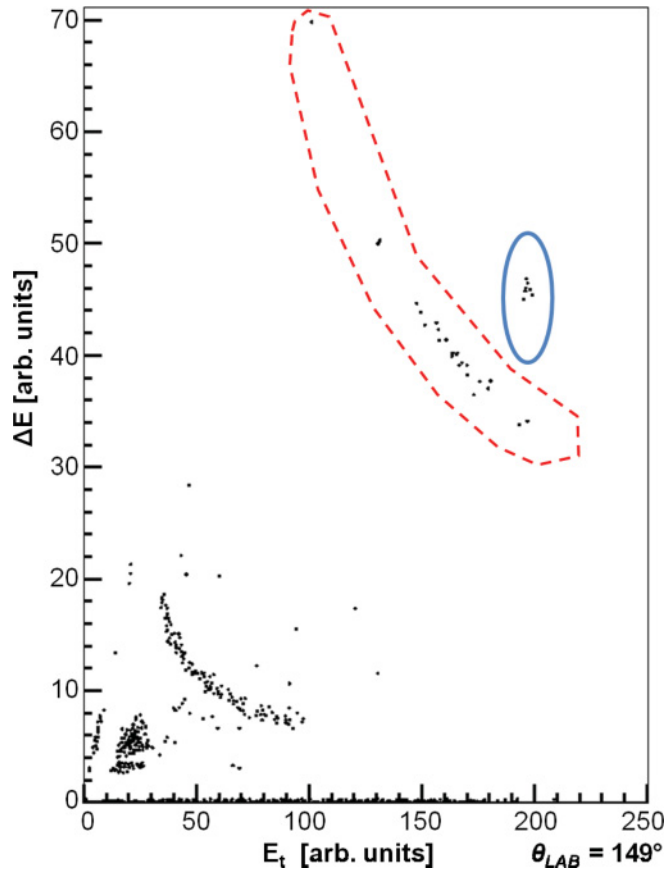

FIG. 3. (Color online) Typical particle identification spectrum ΔE-E_t of one strip from the CD-backward telescope, obtained with the ^{6}He beam at $E_{\mathrm{LAB}} = 22$ MeV. The solid line ellipsoid encloses events corresponding to elastically scattered ^{6}He. The dashed polygon encloses ^{4}He fragments (see text for details).

In each case, it was possible to achieve mass and charge separation of the charged reaction fragments with standard energy-loss techniques.

A typical particle identification spectrum ΔE-E_t (where ΔE is the energy signal registered in the ΔE detector and E_t is the sum of the energy signals registered in both detectors of the telescope) obtained in a CD-forward telescope is shown in Fig. 2. One should notice the good separation obtained between ^{6}He and ^{4}He as well as that between ^{4}He and lighter hydrogen isotopes. Three different regions of interest are identified: ^{6}He resulting from elastic scattering on the ^{208}Pb target, ^{6}He scattered in the collimators placed upstream of the reaction chamber, and ^{4}He yield produced in collisions of the ^{6}He beam, both with the ^{208}Pb target and with the collimators.

A typical particle identification spectrum ΔE-E_t obtained in a CD-backward telescope is shown in Fig. 3. In the same way as described above, events related to the elastically scattered ^{6}He on the target and the ^{4}He yield can be observed. However, in this angular region the scattering and fragmentation of the projectiles on the collimators are not present.

Finally, Fig. 4 shows two typical ΔE-E_t calibrated spectra from a square-forward telescope [Fig. 4(a)] and a square-backward telescope [Fig. 4(b)]. As shown in Fig. 4, despite the square telescopes being located on opposite sides of the

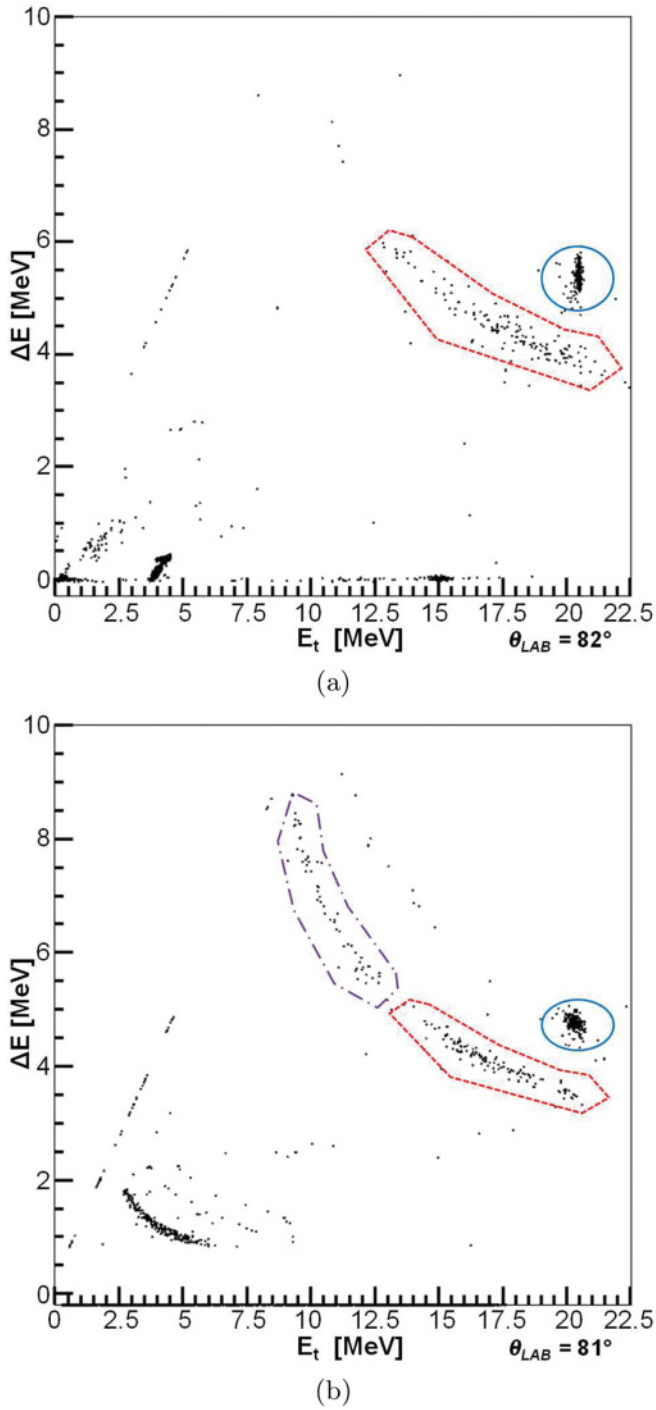

FIG. 4. (Color online) Typical particle identification spectra ΔE-E_t of two strips from the square telescopes, obtained with the ^{6}He beam at $E_{\rm LAB} = 22$ MeV: (a) square-forward telescope; (b) square-backward telescope. In both histograms the solid line ellipsoid encloses elastically scattered ^{6}He, while dashed and dot-dashed polygons enclose ^{4}He fragments (see text for details).

target, the observation angle of both telescopes is overlapping, and it is possible to compare the obtained spectra. The square-backward telescope [Fig. 4(b)] shows ^{4}He events at energy $E < 13$ MeV due to scattering on the aluminium of the target frame. These are not present in the square-forward

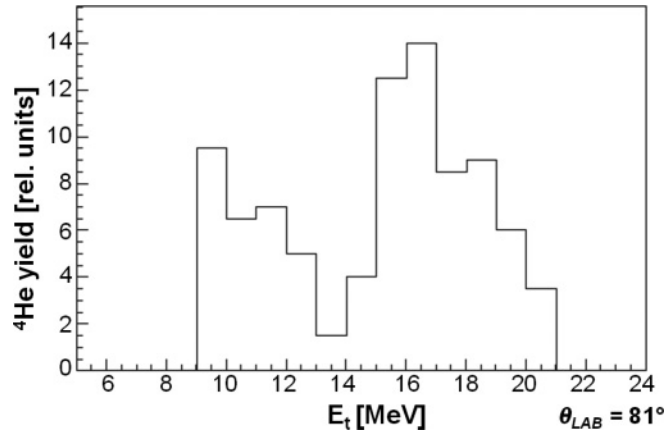

FIG. 5. ^{4}He yield as a function of the total energy (at $\theta_{\rm LAB} = 81^\circ$). The low-energy region is not related to the studied reaction. The high-energy region shows the α-particle yield produced in ^{6}He + ^{208}Pb collisions (see text for details).

telescope because the beam, which is slightly off-center, only hit the side of the frame facing the backward detectors. We have confirmed this hypothesis by a detailed examination of the CD-backward telescopes data.

The small overlap between both distributions (see Fig. 5) allowed us to separate the relevant ^{4}He yield at high energies in all the telescopes where this effect was observed.

B. Elastic scattering

Elastic scattering yields for both measurements (with the ^{6}He beam and with the ^{4}He beam) were obtained by integrating the corresponding peak for each detector. The dead-time correction was determined by the number of recorded pulser events. Also the scale factor due to the rate divider (see Sec. II) was taken into account in the ^{4}He case.

As shown in Sec. II, a fraction of the beam was striking the target frame, which means that the beam was off-center at the position of the target. In this context, the beam misalignment effect on the scattering and solid angles was studied by applying the same method used in Refs. [4,6], and an effective position (x, y) of the beam in the target was calculated. In this way, the effective scattering and solid angles for each individual strip were obtained. The key condition for the application of the method is to get measurements at angles such that Rutherford scattering occurs. This condition is accomplished in the CD-forward telescopes. In addition, the elastic cross section varies rapidly by orders of magnitude in the small angular region covered by the CD-forward telescopes, ensuring an appropriate convergence of the algorithm used in the method. The beam misalignment was studied in the ^{4}He and ^{6}He cases.

The ratio between elastic cross section and the Rutherford cross section, once the corrections for misalignment are considered, is as follows:

$$\frac{\sigma_{\rm el}}{\sigma_R}(E,\theta) \equiv \frac{\frac{d\sigma_{\rm el}}{d\Omega}(E,\theta)}{\frac{d\sigma_R}{d\Omega}(E,\theta)} = C(E) \times \frac{N_{\rm el}(E,i)}{N_R(E_0,i)} \times F(E,i), \quad (1)$$

where $C(E)$ is a normalization constant, $N_{\rm el}(E,\theta)$ is the yield of ^{6}He elastic events at the laboratory energy $E = 22$ MeV and telescope i, corresponding to center-of-mass (c.m.) angle θ, and $N_R(E_0, i)$ is the yield of ^{4}He elastic events at the laboratory energy $E_0 = 12$ MeV in the same strip. $F(E, i)$ accounts for the correction due to beam misalignment. The value for the normalization constant $C(E)$ was calculated so that the average of the ratio at small angles ($<20^\circ$) is 1.

Uncertainties in the observation angles have been calculated by considering the distance between the target and the ΔE detectors, the angle that the target was tilted, and its size. The contribution due to the strip size is negligible compared to the size of the target.

For the final angular distributions (presented in Sec. IV A), the average of the ratios resulting from Eq. (1) in every ring of the CD-forward and CD-backward telescopes was computed. Equivalent ratios using the data registered on the square telescopes were also obtained. In this case, the angular position for each vertical strip was calculated by taking into account the angular correction made for forward and backward CD telescopes.

C. ^{4}He production

Figures 2–4 show typical ΔE-E_t two-dimensional plots in each of the three different sections of the setup. It can be seen that the α-particle events are clearly identified. For the telescopes upstream of the target, ^{4}He reaction fragments resulting from the interaction of ^{6}He projectiles with the target frame (low-energy distribution) as well as with the target (high-energy distribution) were registered, as explained in Sec. III A. The x projection of the ΔE-E_t spectrum in Fig. 4(b) is shown in Fig. 5, where the yield of the relevant ^{4}He events of the distribution at high energy can be easily calculated.

Once the selection of valid ^{4}He events is performed as described above, the ^{4}He yield produced in ^{6}He + ^{208}Pb collisions was divided by the elastic yield in ^{6}He + ^{208}Pb collisions for every strip. The resulting angular distribution gives the ratio of the ^{4}He production cross section over the elastic cross section in ^{6}He + ^{208}Pb collisions. It is important for the interpretation to remark that contributions from different ^{4}He production mechanisms are included in the cross section, since only charged fragments were registered. On the experimental side, no further corrections need to be considered regarding the quotient, since systematic errors cancel.

IV. EXPERIMENTAL RESULTS

A. Elastic scattering

In Fig. 6 we present our experimental differential cross sections for the elastic scattering at 22 MeV in the c.m. reference frame (circles). These data are compared with data from Ref. [6] (triangles). A good agreement between the two experimental datasets is observed.

The differential elastic cross sections follow the Rutherford cross section at small angles and decrease in a monotonic and smooth way when the scattering angle increases. The situation

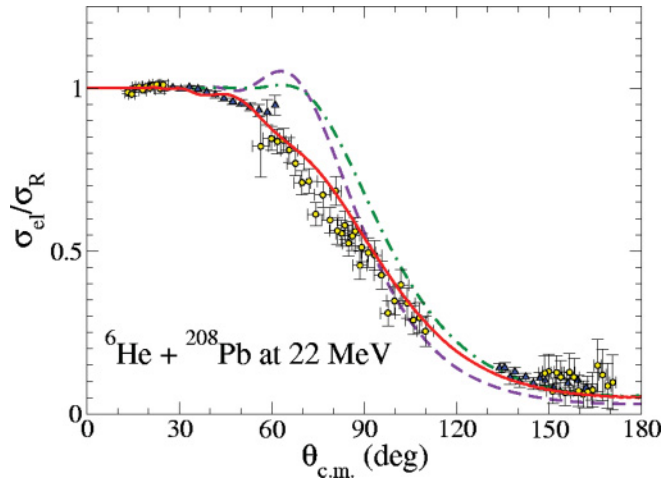

FIG. 6. (Color online) Angular distributions, relative to the Rutherford cross section, for the elastic scattering of ^{6}He on ^{208}Pb at $E_{\rm LAB}$ = 22 MeV. The present data (circles) are compared with previous data (triangles) from Ref. [6] as well as three calculations (see text for details).

is completely different in ^{6}Li scattering at similar energies [16], where the angular distribution shows an interference pattern of the Fresnel type, characterized by the Coulomb rainbow. In the ^{6}He scattering case, the data show no rainbow. In Refs. [4,6,17,18] experimental data on elastic scattering of ^{6}He around the Coulomb barrier are modeled by optical model calculations. These works needed an imaginary diffuseness greater than 1.6 fm, which is appreciably higher than the typical value (0.65 fm) for stable heavy-ion scattering. This result suggests the presence of reaction channels taking place at distances further than 18 fm, as shown in Ref. [6]. This behavior is a common feature for weakly bound nuclei, mainly in collisions with heavy targets, also found in Refs. [5,19,20] for the case of ^{6}He, and in Refs. [21,22] dealing with ^{11}Be scattering.

Our elastic distribution has been compared with three-body CDCC calculations [8], using a simple dineutron model for the ^{6}He nucleus developed in Ref. [9]. In this model, the ^{6}He ground-state wave function is calculated by assuming an effective $2n$-^{4}He separation energy of $\varepsilon_b = -1.6$ MeV. The $\alpha + 2n$ relative wave function for the ^{6}He ground state (g.s.) is assumed to correspond to a pure $2S$ configuration, which is in fact the dominant configuration according to the predictions of three-body models [23]. The $\alpha + 2n$ interaction was parametrized in terms of a Woods-Saxon potential with radius $R = 1.9$ fm and diffuseness $a = 0.39$ fm. We consider $l = 0, 1,$ and 2 partial waves for the ^{6}He continuum. To generate the continuum states, the same potential geometry as for the g.s. was used. For $l = 0$ continuum states, the same depth found for the g.s. was used. For $l = 2$, the potential depth was adjusted in order to get the 2^+ resonance at the correct excitation energy with respect to the g.s. For $l = 1$ continuum, the depth obtained for $l = 2$ was adopted.

The fragment-target interactions, required to generate the projectile-target coupling potentials, were represented by optical potentials evaluated at the appropriate energy. For the

$2n$-^{208}Pb interaction the potential of Perey and Perey [24] was used, whereas the $\alpha + {}^{208}$Pb system was described with the optical potential reported in Ref. [25].

The result of the calculation described above, shown in Fig. 6 with a solid line, explains fairly well the overall trend of the experimental data, given that no parameter is fitted in the calculation. The comparison of this calculation and the one depicted as a dot-dashed line in Fig. 6, with omitted dipole couplings, reveals the importance of the coupling with the continuum states by means of the dipole operator. This results in a reduction of the elastic cross section of about 10% in the rainbow angular region.

In addition, the calculation with the omitted coupling to the continuum predicts an angular distribution similar to that obtained for ^{6}Li in Ref. [16], where the whole rainbow is observed (dashed line in Fig. 6).

B. Alpha-particle production

In the present work the angular distribution of α particles emitted in the scattering of ^{6}He at Coulomb energies has been measured for a wide angular range. As mentioned in Sec. III C, inclusive measurements of the ^{4}He production cross sections are considered in this study. In this respect, the data presented here impose fewer constraints for their interpretation than those reported in Refs. [26,27], where exclusive measurements of emitted ^{4}He and neutrons were performed. On the other hand, the covered angular region in those works were appreciably more limited.

Our experimental results obtained for α-particle production are shown in Fig. 7 (circles). The ratio between ^{4}He yield and elastic yield in ^{6}He + ^{208}Pb collisions as a function of the scattering angle in the laboratory system is shown (top panel). We compare these results with those for the same system and at the same energy published in Ref. [7] (triangles) covering only backward angles from 130° to 170°. The two angular distributions agree in the region of overlap.

The experimental results indicate an α-particle yield ten times greater than the elastic scattering yield at backward angles, and similar yields are evident at angles around 80°. Comparing the ^{4}He differential cross sections shown in Fig. 7 (bottom panel) with those reported in Ref. [19], for a similar reaction at the same energy, we found that the data are consistent, particularly at $\theta > 90°$.

Among the three scenarios that we consider in previous works [7,28] (i.e., dineutron transfer to the continuum, direct breakup, and one-neutron transfer), we study here the ability of dineutron transfer to explain the α particles at the intermediate angles measured in the present experiment. According to Refs. [7,10,19] the large yield of α particles observed at large angles can be attributed to this mechanism. Following Ref. [7], the two-neutron transfer has been treated within the DWBA, including the transition to a set of doorway final states for the ^{210}Pb nucleus. The ^{6}He ground state is treated within the same dineutron model used in the CDCC calculations of the previous section. Doing this, we find that the α-dineutron wave function is similar to a realistic three-body model [23].

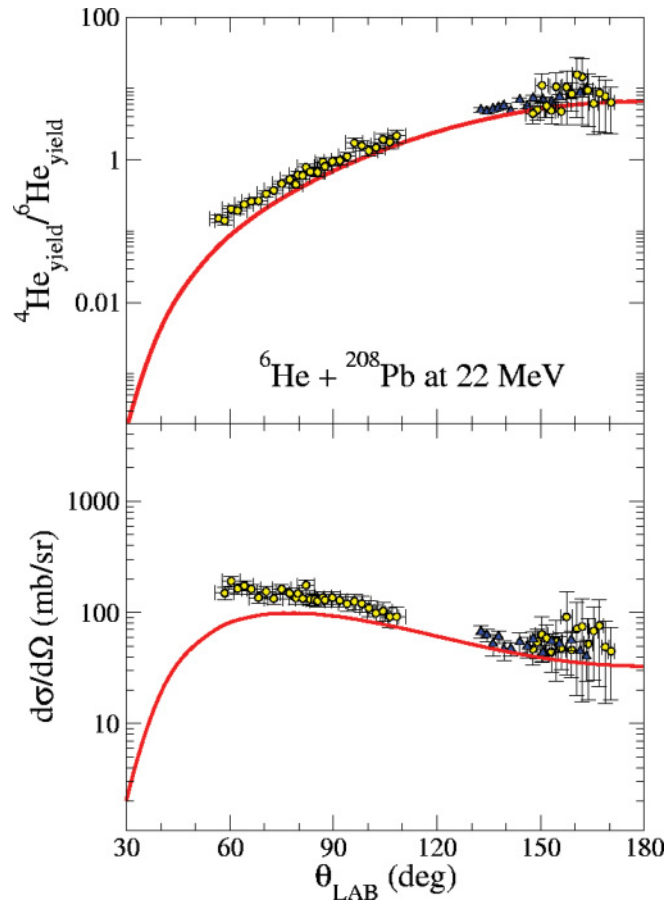

FIG. 7. (Color online) Top: Angular distribution of α-particle production relative to elastically scattered ^{6}He in collisions with ^{208}Pb at 22 MeV. The data (circles) are compared with previous data (triangles) from Ref. [7]. A DWBA calculation is also included in the plot (solid line). Bottom: The differential cross section of α-particle production as a function of $\theta_{\rm LAB}$. The values for this observable resulting from the same DWBA calculation and data from Ref. [7] are also shown. See text for details.

The calculation proposed (solid curve in Fig. 7) was generated using six partial waves to the relative motion of $2n$-Pb, a maximum value for the total angular momentum of $J_{\rm max} = 50$, and a maximum integration radius of 80 fm. The parameters of the optical potential were obtained by means of an optical model calculation fitted to the elastic data shown in Fig. 6. For the model used we assumed a two-neutron transfer mechanism. The $2n$-α potential used was the one reported in Ref. [8], while for the fragment-target interactions the potential used for the $2n + {}^{208}$Pb interaction was taken from Ref. [24]. For the $\alpha + {}^{208}$Pb system, the optical potential of Barnett and Lilley [29] was used and this was also employed for the $\alpha + {}^{210}$Pb potential, keeping the same reduced radius.

This model displays an acceptable agreement with most of the experimental results shown in Fig. 7. The calculation slightly overestimates the experimental data reported at smaller angles (∼55°–75°). This difference can be due mainly to one-neutron transfer [27,30], which is not considered in the DWBA calculation presented here. According to the results

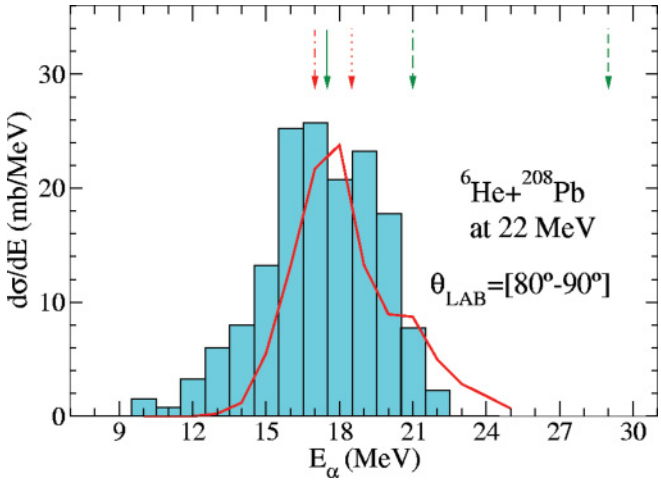

FIG. 8. (Color online) Experimental energy distribution of the produced ^{4}He (bars) for the angular range $80^\circ < \theta_{\rm LAB} < 90^\circ$ compared with a DWBA calculation where transfer to the continuum is considered (solid line). The arrows indicate the expected energy of the scattered ^{4}He at $\theta_{\rm LAB} = 85^\circ$, assuming (i) $1n$-transfer (dotted line corresponding to Q_{gg} and dot-dashed to zero Q value); (ii) $2n$-transfer (dashed line corresponding to Q_{gg}, long dashed line to zero Q value, and solid line to $Q = -4$ MeV).

presented in [26], the direct breakup effect for this angular range is very small compared with transfer processes. Hence one-neutron transfer is another mechanism that can contribute significantly in this angular region, as was shown in the calculations presented in Ref. [7].

Despite some possible contribution of the one-neutron transfer mechanism, the angular and energy distribution of α particles can be mainly explained by assuming a two-neutron transfer mechanism, leading to both bound and unbound states of the residual nucleus (^{210}Pb). This can also be observed in the plot shown in Fig. 8, where the experimental energy distribution of the α particles for the angular range from 80° to 90° is depicted and compared with the transfer calculation. The calculation suggests that the dominant process is the two-neutron transfer, as was found in Ref. [7] where the data were limited to angles $> 130^\circ$. The present data show that the same mechanism remains dominant at intermediate angles with a Q value of ~ -4 MeV, according to Fig. 8. The results in Ref. [7] also suggest a negative optimum Q value. Additionally, an optimum Q value of ~ -3 MeV was reported in Ref. [31] for the two-neutron transfer reaction ^{118}Sn(^{18}O,^{16}O)^{120}Sn.

V. SUMMARY AND CONCLUSIONS

Data for the reaction ^{6}He + ^{208}Pb measured at $E_{\rm LAB} = 22$ MeV have been presented. The data include a full angular distribution of the elastic cross section and the α-particle production from the interaction between projectile and target. These results complement the data of a previous experiment, presented in Refs. [6,7], that covered a more restricted angular range.

Three-body CDCC calculations, using an improved two-body model of ^{6}He, have been found to reproduce the experimental elastic data reasonably well. It has confirmed that the coupling with continuum states by means of the electric dipole operator has to be considered to reproduce the strong absorption effect, as was found previously in Refs. [4–6]. In order to accurately describe this phenomenon it would be necessary to use a four-body scattering model (the three-body projectile and the target) [32,33]. We believe, however, that the simpler three-body reaction model used is sufficient to understand the main features of the experimental results, considering the good agreement with the data, and the fact that the three-body CDCC calculations, based on a suitable two-body model of ^{6}He, have been found to reproduce pretty well the elastic cross sections provided by more sophisticated four-body CDCC calculations, at least for heavy targets [9].

In addition, α-particle production was measured in the angular range $\theta_{\rm LAB} = [55^\circ, 170^\circ]$, at an energy around the Coulomb barrier. The obtained data were compared with previous experimental results [7], covering only the 130°–170° (backward) angular range, and good agreement was obtained. We have performed DBWA calculations, in which the α particles are assumed to arise from a two-neutron transfer mechanism, leading to bound and unbound states of the final nucleus (^{210}Pb). These calculations describe the data in a suitable way for the measured angular range ($\theta_{\rm LAB} = 55^\circ$–$165^\circ$), suggesting that this is the dominant mechanism in this region. This was further confirmed by the energy distribution in the angular range of 80°–90°.

With these data it is possible to corroborate unambiguously the previous conclusions induced from data in a reduced angular range on the elastic scattering analysis presented in Refs. [4–6], i.e., the suppression of the Coulomb rainbow and the presence of a long-range absorptive component in the optical potential, required to reproduce the angular distribution of the elastic cross section. In addition, the analysis of α-particle production, studied previously in Refs. [7,19,20], shows that the two-neutron transfer mechanism can also explain the production of α particles at intermediate angles, where the competition between direct breakup and transfer mechanisms is expected. Our data suggest that most of the α-particle yield in a large angular range is linked to neutron transfer mechanisms.

ACKNOWLEDGMENTS

This work has been supported by the Spanish MICINN under projects FPA2005-04460, FPA200502379, FPA2006-13807-c02-01, FPA2007-63074, FPA2009-07653, FPA2009-07387 and FPA2010 22131-C02-01, by the Junta de Andalucía project FQM-4964, by the Spanish Consolider-Ingenio 2010 Programme CPAN (CSD2007-00042) and Programme Multi-Dark (CSD2009-00064), by the European Community-Access to Research Infrastructure action of the Improving Human Potential Program Contract, No. HPRI-CT-1999-00110, and by the Belgian Program P5/07 on interuniversity attraction poles of the Belgian-state Federal Services for Scientific, Technical and Cultural Affairs. L. Acosta acknowledges financial support by the Universidad de Huelva.

[1] P. G. Hansen and B. Jonson, Europhys. Lett. **4**, 409 (1987).
[2] K. Katō, S. Aoyama, S. Mukai, and K. Ikeda, Nucl. Phys. A **588**, c29 (1995).
[3] T. Kobayashi, O. Yamakawa, K. Omata, K. Sugimoto, T. Shimoda, N. Takahashi, and I. Tanihata, Phys. Rev. Lett. **60**, 2599 (1988).
[4] O. R. Kakuee *et al.*, Nucl. Phys. A **728**, 339 (2003).
[5] O. R. Kakuee *et al.*, Nucl. Phys. A **765**, 294 (2006).
[6] A. M. Sánchez-Benítez *et al.*, Nucl. Phys. A **803**, 30 (2008).
[7] D. Escrig *et al.*, Nucl. Phys. A **792**, 2 (2007).
[8] K. Rusek, I. Martel, J. Gomez-Camacho, A. M. Moro, and R. Raabe, Phys. Rev. C **72**, 037603 (2005).
[9] A. M. Moro, K. Rusek, J. M. Arias, J. Gómez-Camacho, and M. Rodríguez-Gallardo, Phys. Rev. C **75**, 064607 (2007).
[10] J. P. Fernández-García *et al.*, Phys. Lett. B **693**, 310 (2010).
[11] G. Ryckewaert *et al.*, Nucl. Phys. A **701**, 323 (2002).
[12] D. Miljanić *et al.*, Nucl. Instrum. Methods Phys. Res., Sect. A **447**, 554 (2002).
[13] [http://www.uhu.es/gem/dinex/dinex.htm].
[14] A. M. Sánchez-Benítez *et al.*, J. Phys. G: Nucl. Part. Phys. **31**, S1953 (2005).
[15] L. Acosta [http://hdl.handle.net/10272/2794].
[16] N. Keeley *et al.*, Nucl. Phys. A **571**, 326 (1994).
[17] E. F. Aguilera *et al.*, Phys. Rev. C **63**, 061603(R) (2001).
[18] J. P. Fernández-García *et al.*, Nucl. Phys. A **840**, 19 (2010).
[19] E. F. Aguilera *et al.*, Phys. Rev. Lett. **84**, 5058 (2000).
[20] A. Di Pietro *et al.*, Phys. Rev. C **69**, 044613 (2004).
[21] L. Acosta *et al.*, Eur. Phys. J. A **42**, 461 (2009).
[22] A. Di Pietro *et al.*, Phys. Rev. Lett. **105**, 022701 (2010).
[23] A. Cobis, D. V. Fedorov, and A. S. Jensen, Phys. Rev. Lett. **79**, 2411 (1997).
[24] C. M. Perey and F. G. Perey, Phys. Rev. C **132**, 755 (1963).
[25] G. Goldring *et al.*, Phys. Lett. B **32**, 465 (1970).
[26] J. J. Kolata *et al.*, Phys. Rev. C **75**, 031302(R) (2007).
[27] Chatterjee *et al.*, Phys. Rev. Lett. **101**, 032701 (2008).
[28] A. M. Moro *et al.*, AIP Conf. Proc. **1139**, 7 (2009).
[29] A. R. Barnett and J. S. Lilley, Phys. Rev. C **9**, 2010 (1974).
[30] P. A. De Young *et al.*, Phys. Rev. C **71**, 051601(R) (2005).
[31] W. Henning, Y. Eisen, H. J. Korner, D. G. Kovar, J. P. Schiffer, S. Vigdor, and B. Zeidman, Phys. Rev. C **17**, 2245 (1978).
[32] M. Rodriguez-Gallardo, J. M. Arias, J. Gomez-Camacho, R. C. Johnson, A. M. Moro, I. J. Thompson, and J. A. Tostevin, Phys. Rev. C **77**, 064609 (2008).
[33] M. Rodriguez-Gallardo, J. M. Arias, J. Gomez-Camacho, A. M. Moro, I. J. Thompson, and J. A. Tostevin, Phys. Rev. C **80**, 051601(R) (2009).